RNA at the surface of phase-separated condensates impacts their size and number

Audrey Cochard, Marina Garcia-Jove Navarro, Leonard Piroska, Shunnichi Kashida, Michel Kress, Dominique Weil, Zoher Gueroui

▶ **To cite this version:**

Audrey Cochard, Marina Garcia-Jove Navarro, Leonard Piroska, Shunnichi Kashida, Michel Kress, et al.. RNA at the surface of phase-separated condensates impacts their size and number. Biophysical Journal, 2021, 121 (9), pp.1675-1690. 10.1016/j.bpj.2022.03.032 . hal-03767229

HAL Id: hal-03767229
https://hal.science/hal-03767229

Submitted on 20 Sep 2022

HAL is a multi-disciplinary open access archive for the deposit and dissemination of scientific research documents, whether they are published or not. The documents may come from teaching and research institutions in France or abroad, or from public or private research centers.

L'archive ouverte pluridisciplinaire **HAL**, est destinée au dépôt et à la diffusion de documents scientifiques de niveau recherche, publiés ou non, émanant des établissements d'enseignement et de recherche français ou étrangers, des laboratoires publics ou privés.

RNA at the surface of phase-separated condensates impacts their size and number

Audrey Cochard[1,2], Marina Garcia-Jove Navarro[1], Leonard Piroska[1], Shunnichi Kashida[1], Michel Kress[2], Dominique Weil[2]*, Zoher Gueroui[1]*

1- PASTEUR, Department of Chemistry, École Normale Supérieure, PSL University, Sorbonne Université, CNRS, 75005 Paris, France.

2- Sorbonne Université, CNRS, Institut de Biologie Paris-Seine (IBPS), Laboratoire de Biologie du Développement, F-75005 Paris, France.

*Correspondence: zoher.gueroui@ens.fr, dominique.weil@upmc.fr

ABSTRACT

While it is now recognized that specific RNAs and protein families are critical for the biogenesis of ribonucleoprotein (RNP) condensates, how these molecular constituents determine condensate size and morphology is unknown. To circumvent the biochemical complexity of endogenous RNP condensates, the use of programmable tools to reconstitute condensate formation with minimal constituents can be instrumental. Here we report a methodology to form RNA-containing condensates in living cells programmed to specifically recruit a single RNA species. Our bioengineered condensates are made of ArtiGranule scaffolds composed of an orthogonal protein that can bind to a specific heterologously expressed RNA. These scaffolds undergo liquid-liquid phase separation in cells and can be chemically controlled to prevent condensation or to trigger condensate dissolution. We found that the targeted RNAs localize at the condensate surface, either as isolated RNA molecules or as a homogenous corona of RNA molecules around the condensate. The recruitment of RNA changes the material properties of condensates by hardening the condensate body. Moreover, the condensate size scales with RNA surface density; the higher the RNA density, the smaller and more frequent the condensates. These results suggest a mechanism based on physical constraints, provided by RNAs at the condensate surface, that limit condensate growth and coalescence.

Statement of Significance

It is increasingly recognized that biomolecular condensates contribute to organize cellular biochemistry by concentrating and compartmentalizing proteins and nucleic acids. How molecular constituents of condensates determine their size and morphology is unknown. To circumvent the biochemical complexity of endogenous RNP condensates, the use of programmable tools to reconstitute condensate formation with minimal constituents can be instrumental. Here we report a methodology to form RNA-containing condensates in living cells programmed to specifically recruit a single RNA species. These ArtiGranule scaffolds undergo liquid-liquid phase separation in cells and can be chemically controlled to prevent condensation or to trigger condensate dissolution. Using this tool, we found that the condensate size scales with RNA surface density. This observation can be explained by physical constraints limiting condensate growth and coalescence.

INTRODUCTION

It is increasingly recognized that biomolecular condensates contribute to organize cellular biochemistry by concentrating and compartmentalizing proteins and nucleic acids. They include a broad range of nuclear and cytoplasmic ribonucleoprotein (RNP) granules, such as nucleoli, P-bodies (PBs), germ granules and stress granules (SGs). Remarkably, abnormal condensate maturation into toxic aggregates is linked to viral infection, cancer, and neurodegenerative diseases (1). Cellular condensates harbour a large diversity in terms of biochemical composition as well as functions. Nevertheless, a unified model of formation via liquid-liquid phase separation (LLPS), where RNP constituents interact through multivalent and weak interactions, has been proposed to understand their biogenesis (2–6). In addition to their diverse compositions and functions, condensates are also diverse in size. While PBs or PML bodies are often diffraction-limited puncta, other condensates such as germ granules, centrosomes, and nucleoli can reach few micrometres in size (2, 7–10). What sets condensate size and number in cells remains to be understood.

Mounting evidence based on *in vitro* reconstitutions and cellular approaches underlined the importance of multivalent interactions between RNA-binding proteins (RBPs) and RNAs in shaping condensate biogenesis and morphology. In particular, RNA molecules have been shown to play fundamental roles in determining the structure, dynamic and biophysical properties of condensates (11). For instance, RNAs act as molecular seeds to nucleate phase-separated condensates and regulate their assembly in a spatiotemporal manner (12–17). On the opposite, high RNA concentration can dissolve condensates and keep prion-like RBPs soluble in the cell nucleus (18, 19). In addition to their formation or dissolution, RNA molecules can also impact the viscosity of the RNP condensates and the dynamics of their components in a sequence-dependent manner (20–22). The different structures of RNAs can also determine the molecular specificity of RNP condensates and thus explain the coexistence of separate condensates with distinct molecular compositions (23). Moreover, when RNAs are unstructured, RNA-RNA interactions can lead to the formation of non-spherical condensates (24). Finally, RNAs can take part in RNA-RBP interactions that drive the formation of multiphase condensates, whose structure relies on RNA concentration and on RNA-RBP interaction strength (22, 25, 26). In addition to the contribution of condensate constituents, extrinsic factors such as membrane, cytoskeleton and chromatin can modulate LLPS and condensate biogenesis and coarsening (27–29).

Several bioengineering approaches have recently been developed to form condensates with specific properties in cells, and thus combine the control of condensate components achievable in *in vitro* experiments with the possibility to study LLPS within the cellular environment. These approaches often use optogenetic and chemical actuations based on protein-multimerization domains

acting as scaffolds of artificial condensates. Engineering them with well-defined compositions, structures and dynamic properties provides novel tools to correlate condensate biochemical functions with their material states, a link that is still difficult to reach by studying native RNP condensates. Such methods thus enabled quantitative studies of the dynamical properties of phase-separated condensates within cytoplasm and nucleus. For example, light-induced strategies based on optoDroplets allowed the actuation of model condensates that mimic pathological assemblies appearing in some age-related diseases (30, 31). Alternative synthetic protein condensates were also designed with programmable material properties or functions (32–39). As a model for RNP condensates, iPOLYMER, Corelet, and our ArtiGranules (ArtiGs) were designed to induce condensation of RNA-binding motifs found in SGs (TIA-1, G3BP1) and PBs (Pumilio), respectively (40–42). While these approaches provided a powerful mean to manipulate RNP condensate mimics in cells, they used RBP motifs that can bind thousands of RNA species, which could considerably limit our ability to interpret resulting observations in cells.

To overcome the inherent biochemical complexity of RBP containing artificial condensates, our strategy has consisted in building a minimal RNP condensate, composed solely of an orthogonal protein that can bind a specific heterologously expressed RNA. To this aim, we relied on the widely used MCP/MS2 system, where MCP is the coat protein of the MS2 bacteriophage, which binds with high specificity and affinity to RNA stem loops of its genome, referred to as MS2 (43). We fused MCP to our previously developed ferritin-based ArtiG scaffold (42)**.** When expressed in HeLa cells, the resulting ArtiG^{MCP} scaffolds underwent LLPS and formed micrometric bodies within the cytoplasm. When co-expressed with MS2-containing RNAs (MS2-RNAs), all condensates were decorated by MS2-RNA molecules. We found that MS2-RNAs localized at the condensate surface, either as isolated RNA molecules or as a homogenous corona of RNA molecules around the condensate. Furthermore, fluorescent recovery after photobleaching experiments showed that RNA induced a hardening of the condensates towards a gel phase. We also found that cytosolic MS2-RNAs were depleted at the vicinity of large condensates, within a few micrometer range. The ArtiG^{MCP} condensates remained distinct from endogenous condensates, such as PBs or SGs. The assembly of ArtiG^{MCP} condensates is reversible: addition of a binding competitor of the self-interacting protein scaffolds enabled both dissolution and impediment of formation with a high efficiency. We first observed a negative correlation between the number of ArtiG condensates per cell and their mean diameter. The possibility to detect each individual RNA-MS2 molecule then allowed to quantitatively link RNA density to condensate size, which is not feasible for native condensates that recruit a large variety of RNAs. By quantifying the localization and number of individual RNA-MS2 molecules, we found that the higher the RNA density, the smaller and more numerous the condensates. Overall, our

data indicated that the size of RNP condensate scales down with RNA surface density, which can be explained by physical constraints limiting condensate growth and coalescence.

MATERIALS AND METHODS

Experimental model

Human epithelioid carcinoma HeLa (ATCC, ccl-2) and embryonic kidney HEK-293 (ATCC, CRL-1573) cells were maintained in Dulbecco's modified Eagle's medium (with 4.5 g/L D-glucose, HyClone) supplemented with 10% fetal bovine serum (Gibco, 10270106) and antibiotics, at 37 °C in a 5% CO2 humidified atmosphere. Cells were routinely tested for mycoplasma contamination.
SGs were induced with 0.5 mM sodium arsenite (Sigma) for 30 min at 37°C.
For inhibition and reversibility experiments (Fig. 3B-E), 2.5 µM of FK506 (Sigma F4679) was added to the cell culture medium.

Plasmids

All constructs were sub-cloned into pcDNA 3.1 plasmid (Invitrogen). The plasmids pcDNA3.1-F36M-FKBP(Fm)-emGFP-hFt, Fm-mCh-hFt and pcDNA3.1–Fm–hFt were previously described (42). The plasmid pcDNA3.1–Fm–MCP–hFt was obtained by replacing the emGFP CDS between XhoI and BamHI restriction sites in pcDNA3.1–Fm–emGFP–hFt by a CDS encoding a tandem of two MS2-coat proteins (MCP). We used a tandem to enhance binding to MS2 stem loops (44). All three above-mentioned plasmids contain a 6xHis sequence. RNA-MS2 was expressed from the plasmid pcDNA3.1–4xMS2, which was obtained by inserting the iRFP CDS in the pcDNA3.1 backbone along with a tandem of four MS2 stem loops in the 3'UTR.
The plasmid for cytoplasmic poly(A)-binding protein (PABP-GFP) expression is a gift from M. W. Hentze (45).

Transfection

For live experiments, HeLa cells were cultured on 35 mm µ-dishes with polymer coverslip bottom (ibidi, 1.5 x 10^5 cells/µ-dish). For other experiments, HeLa cells and HEK-293 cells were cultured on 22x22 mm glass coverslips (VWR) in 6-well plates (Falcon, 3.5 x 10^5 cells/well). 24 h after seeding, transient transfection using Lipofectamine 2000 (Invitrogen) was carried out according to the manufacturer's protocol. For live experiments, cells were transfected with a 1:1 ratio of pcDNA3.1–Fm–MCP–hFt and pcDNA3.1–Fm–emGFP–hFt (800 ng total per µ-dish) and 20 ng of pcDNA3.1–4xMS2. For other experiments, cells were transfected with a 1:0.7:0.3 ratio of pcDNA3.1–Fm–MCP–hFt, pcDNA3.1–Fm–emGFP–hFt and pcDNA3.1–Fm–hFt (2 µg total per well) and 50 ng (low RNA),

250 ng (high RNA) or indicated amount (Fig. S2B) of pcDNA3.1–4xMS2. For PABP-GFP co-transfection experiment, the same plasmid ratio was transfected, with Fm-mCh-hFt instead of Fm-emGFP-hFt, along with 500 ng of the PABP-GFP plasmid.

Single molecule Fluorescence In Situ Hybridization (smFISH)

Single RNA molecule detection was performed according to the previously described smiFISH (single molecule inexpensive FISH) method (46). For each target RNA (RNA-MS2, β-actin mRNA and NORAD lncRNA), a set of 24 primary probes, composed of a distinct sequence and a common FLAP sequence (TTACACTCGGACCTCGTCGACATGCATT), was designed with the Oligostan R script (46). The primary probes and the Cy3 FLAP probe (sequences in the Supplementary table 1) were purchased from Integrated DNA Technologies. An equimolar mixture of the 24 primary probes (initial concentration of 100 µM) was prepared and diluted five times in TE buffer, for a final concentration of individual probes of 0.833 µM.

24h after transfection, cells were fixed in 4% paraformaldehyde (PFA) for 20 min at RT, and permeabilized with 70% ethanol in phosphate buffer saline (PBS) at 4°C overnight. They were then washed once with PBS and incubated for 15 min at RT in 15% formamide freshly prepared in saline-sodium citrate (SSC) buffer. Primary and secondary probe were pre-hybridized by incubating 2 µl of the gene-specific probe set, 1 µl of the Cy3 FLAP probe, 1µl of NEBuffer 3 and 6 µl of water, for 3 min at 85°C, 3 min at 65°C and 5 min at 25°C, successively. Then, two mix were prepared (quantities are given for 6 coverslips): Mix 1 contained 15 µl of 20x SSC buffer, 5.1 µl of 20 µg/µl E. coli tRNA (Merck 10109541001), 45 µl of 100% formamide (Merck F9037), 6 µl of the pre-hybridized probes, and 78.9 µl of water; Mix 2 contained 3 µl of 20 mg/ml Molecular Biology Grade BSA (NEB B9000S), 3 µl of 200 mM VRC (Merck R3380), 63.6 µl of 50% dextran sulphate (Merck S4031) and 80.4 µl of water. Both mixes were vortexed together and 50 µl of the mixture was deposited on each coverslip before hybridization overnight at 37°C in a humidity chamber (a 10 cm Petri dish containing a 3.5 cm Petri dish filled with 1 ml of 15% formamide in SSC buffer). The next day coverslips were washed twice for 30 min at 37°C in 15% formamide in SSC buffer, and rinsed twice in PBS. They were then either mounted with VECTASHIELD mounting medium containing DAPI (Vector Laboratories, H-1200), or processed through immunofluorescence steps.

Immunofluorescence

Cells were permeabilized with PBS 0.1% Triton X-100 for 10 min at RT, washed twice with PBS at RT, incubated with the primary antibody, washed three times with PBS at RT for 5 min, incubated with the secondary antibody, washed three times with PBS at RT for 5 min and finally mounted with VECTASHIELD mounting medium (Vector Laboratories, H-1000). Primary antibodies were rabbit

antibodies against DDX6 (Novus NB200-192, 1:1000 dilution), rabbit antibodies against ATXN2L (Bethyl A301-370A, 1:500 dilution), and rabbit antibodies against MCP (Merck ABE76-I, 1:333 dilution) diluted in PBS 0.1% BSA. The secondary antibody was F(ab')2-Goat anti-Rabbit IgG conjugated with Alexa Fluor 350 dye (Thermo Fisher Scientific A-11069, 1:500 dilution).

Imaging

For live experiments, cells were imaged on a Zeiss LSM 710 META laser scanning confocal microscope using an ×63 oil-immersion objective (PlanApochromatic, numerical aperture (NA) 1.4), at 37°C in a 5% CO2 humidified atmosphere, either starting 8 h after transfection (ArtiG formation) or 24 h after transfection (ArtiG dissolution). Microscope hardware and image acquisition were controlled with LSM Software Zen 2012. Images were analyzed using Fiji (47).

For smFISH experiments, cells were imaged by epifluorescence microscopy performed on an inverted Zeiss Z1 microscope equipped with a motorized stage using a ×63 (NA 1.32) oil-immersion objective. Images were processed with open-source software Fiji and Icy (47, 48).

Fluorescence Recovery After Photobleaching Experiments

FRAP experiments on ArtiG condensates in live HeLa cells were performed starting approximately 20 h after transfection. Bleaching experiments were performed in a humidified chamber maintained at 37°C and 5% CO_2, which was mounted on a Zeiss LSM 710 META laser scanning confocal microscope (using an 63x (NA 1.4) oil immersion objective), and operated with the LSM Zen 2012 software. Each condensate was scanned 10 times in order to establish the average level of initial fluorescence, then bleached using 6 to 10 iterations at 100% 488 nm laser intensity. Subsequently, the fluorescence recovery was monitored using one acquisition per second (512*512 pixel images) for at least 120 s. The region of interest was circular for ArtiG^{emGFP} and ArtiG$^{emGFP/MCP}$, and traced by free-hand selection for the anisotropic ArtiG$^{emGFP/MCP/RNA}$. The average size of the bleached condensates was 2.75 µm (±1.25 µm). FRAP data analysis and fitting of the recovery curves were performed with MATLAB (Mathworks). To determine spatiotemporal FRAP patterns, kymographs were generated by measuring fluorescence evolution as a function of time across a line of interest, using Fiji.

Western Blotting

24 h after transfection, cells were lyzed in Laemmli 1X buffer. Proteins were denatured at 100°C for 5 min. After centrifugation at 15000 g for 10 minutes at 4°C, soluble proteins were quantified using the Coomassie protein assay (Thermo Scientific). 25 µg of proteins were separated on a NuPAGE 4%-12% gel (Invitrogen, Thermo Fisher Scientific) and transferred to an Optitran BA-S83

nitrocellulose membrane (GE Healthcare Life Science). After blockage in PBS with 5% non-fat milk for 30 min, the membrane was incubated with the primary antibody (6x-His Tag Monoclonal Mouse Antibody, Thermo Fisher Scientific MA1-21315; or S6 Ribosomal Protein Rabbit mAb, Cell Signaling 2217) overnight at 4°C. Then the membrane was washed five times for 5 min with PBS, incubated for 30 min in PBS with 5% non-fat milk and then for 1 h at RT with horseradish peroxidase-conjugated secondary anti-mouse antibody (1:10000 dilution in PBS with 5% non-fat milk, Jackson Immunoresearch Laboratories, Anti-Mouse 115 035-003 or Anti-Rabbit 111 035-003), and washed again. Proteins were detected with the chemiluminescence detection reagent Perkin Western Lightning plus ECL (Perkin Elmer) and visualized using a radiology film processor (Curix 60, AGFA).

Data analysis

Detection and counting of RNA molecules was performed using version 0.4.0 of Python package Big-FISH (https://github.com/fish-quant/big-fish) (49). After nucleus segmentation from the DAPI channel, cells were segmented from the Cy3 FISH channel signal with a watershed algorithm. To detect RNA molecules, a Laplacian of Gaussian (LoG) filter was applied to accentuate the spots signal and smooth the background. Then a maximum filter was applied, and local maxima were defined as pixels whose values were not modified by the filter. Local maxima under a threshold (determined by a function of Big-FISH) were considered as background noise and removed, and for each remaining maximum, single point coordinates were extracted. The next step was to detect maxima that could be clusters of RNA molecules and estimate the number of RNAs in those clusters. To do so, the background noise was first removed using a gaussian filter estimation of the background. Then the median spot intensity was computed, set as reference for a single RNA molecule and fitted with a gaussian function. Brighter spots were considered as clusters of RNAs, and the number of RNA molecules in each cluster was estimated based on the single RNA reference intensity.

To count the number of RNAs recruited on condensates in individual cells, a binary mask was first created on the emGFP channel (ArtiGs) using a manually set threshold. RNAs were considered in the condensates if their coordinates were within the mask coordinates.

For the analysis of RNA depletion at the vicinity of condensates (Figures 2 and S3), first the binary mask on the emGFP channel was built as previously. Then it was repeatedly expanded by 5 pixels and RNA molecules in the mask were counted at each step, which enabled the calculation of both the number and the density of RNA molecules in the last incremented area.

Condensate sizes were measured using Icy spot detector (Undecimated Wavelet Transform detector) (50). A lower size limit of 400 nm, corresponding to the diffraction limit of the microscope, was applied to exclude the condensates whose size could not be significantly measured. When close

condensates were not discriminated, the detected regions of interest were adjusted manually. In Figure 5, the size of individual condensates within intertwining clusters that were impossible to quantified were excluded from the statistics of size. For the correlation between condensate size and surface RNA density, the exterior surface was calculated from the condensate maximum projection. Then, for each cell, the sum of the surface of all condensates was calculated and used to determine the mean RNA density at the condensate surface (ratio of the total number of recruited RNAs to the total condensate surface).

Formatting of cell images was performed using the open-source software Fiji (47). For Figure 2 and S3, the RNA coordinates were first saved from the Python workflow and then opened on Fiji. Graphic were generated using the shiny app PlotsOfData (51) (plots in Figure 4B, 4D and 5A) and OriginPro (OriginLab). For all violin plots, circles correspond to the mean. Schemas (Fig. 1A and 5D) were drawn with the open-source vector graphics editor Inkscape.

Statistical analysis

For Figure 3C, Student's t-tests (parametric test to compare two observed means) were performed using the *ttest2* MATLAB function (MathWorks). For Figure 5A, Wilcoxon rank-sum tests (nonparametric test to compare two distributions) were performed using the *ranksum* MATLAB function (MathWorks). For Figure C, Pearson's chi-squared test (nonparametric test for nominal variables) were performed using the Python's chi2_contingency function.

RESULTS

Reconstitution of RNA-protein condensates in human cells

Our first goal was to engineer artificial RNA-protein condensates that assemble through LLPS into cells. Our design combined two parts: a scaffold used to trigger the formation of protein condensates and a grafted RNA-binding domain to recruit specific RNA sequences (Fig. 1A). As protein scaffold, we used ArtiGs that form liquid protein condensates in a concentration-dependent manner through weak multivalent interactions (42). The ArtiG scaffold developed previously was fused to a Pumilio-binding domain that recruits a large number of endogenous Pumilio RNA targets (42). To restrict the targeting to one single RNA species, we chose an orthogonal RNA-binding domain, the MS2-coat protein (MCP), that recognizes specific MS2 stem-loops. The resulting plasmid construct, Fm-MCP-Ft, consisted in the fusion of an oligomeric ferritin (Ft) to MCP and a self-interacting domain F36M-FKBP (Fm), which spontaneously dimerizes without the need of a chemically-induced dimerization molecule such as rapamycin (Fig. 1A) (52).

In order to monitor condensate formation in cells, we co-transfected HeLa cells with the multivalent MCP self-interacting scaffold Fm-MCP-Ft, and Fm-emGFP-Ft as a fluorescent tracer. Live confocal imaging performed 8 h after transfection showed that, initially, emGFP fluorescence at low expression level was diffuse in the cytoplasm. As Fm-emGFP-Ft expression increased, several bright fluorescent bodies nucleated throughout the cytoplasm and grew to reach a micrometric size within an hour (Fig. 1B). The emGFP containing condensates, hereafter called ArtiG$^{emGFP/MCP}$, were very mobile and rapidly grew as a function of time. When two proximal condensates docked, they tended to coalesce and to relax into large spherical bodies, as generally observed for endogenous liquid-like condensates (Fig. 1B, white arrow and Fig. S1A). To reconstitute RNA-protein condensates using ArtiG$^{emGFP/MCP}$, we first generated a plasmid to express a mRNA equipped with MS2 stem-loops in its 3'UTR (1250 nt long, called hereafter RNA-MS2, Fig. 1A). We co-transfected this plasmid (RNA low condition in the methods, i.e. 50 ng) and the plasmids expressing the ArtiG$^{emGFP/MCP}$ scaffold (2 µg) and fixed the cells 24 h after transfection. We next monitored the intracellular localization of RNA-MS2 using single-molecule fluorescence in situ hybridization (smFISH) (46). The majority of cells harbored micrometric ArtiG$^{emGFP/MCP}$ condensates in the cytoplasm, surrounded with a striking Cy3-FISH signal, indicating a localization of RNA-MS2 molecules at the condensate surface (Fig. 1C, insert 1, and Fig. 1E, left panel). These RNAs were either present as isolated molecules or, when the number of recruited molecules was high, were more homogeneously distributed around the condensates, into a corona made of a single RNA molecule layer (see other examples in Fig. S1B). Discrete Cy3 dots corresponding to individual mRNAs were also found dispersed throughout the cytosolic space (Fig. 1C, insert 2), as well as brighter spots in the nucleus corresponding to transcription foci (Fig. 1C, grey arrow). To verify if the RNA corona may result from some enrichment of MCP at the surface of the condensates, we performed an immunostaining of MCP. The antibody labelled the entirety of ArtiG$^{emGFP/MCP}$, indicating a homogeneous distribution of MCP within the condensates (Fig. S1C). The efficient penetration of antibodies into the condensates also suggested that the smaller FISH probes should penetrate as well. Accordingly, rare RNA-MS2 molecules were observed inside condensates, as illustrated in Fig. S1D, where an RNA-MS2 molecule seems to have been trapped during the coalescence of two condensates. Altogether, these results indicate that, despite the presence of MCP within the condensates, the RNA-MS2 molecules are restricted to their surface.

Next, to assess the specificity of RNA recruitment on the ArtiG$^{emGFP/MCP}$, we investigated the localization of RNA-MS2 in cells containing ArtiG^{emGFP} (devoid of the MCP domain) and found a complete absence of RNA-MS2 at the condensate periphery (Fig. 1D, upper panel, and Fig. 1E, middle panel). Experiments carried out in HEK293 cells showed the same results (Fig. S1E and Fig. S1G upper and middle panels). Similarly, ArtiG$^{emGFP/MCP}$ did not show any recruitment of the

endogenous ß-actin mRNA and NORAD lncRNA (devoid of MS2) (Fig. 1D, lower panel, Fig. 1E, right panel, Fig. S1F and Fig. S1G, lower panel). To investigate more broadly the specificity of the RNA recruitment, we co-transfected the plasmids of our artificial condensates with or without RNA-MS2 and with a PABP-GFP plasmid. PABP (Poly-A binding protein), by binding to polyA tails, reports on all polyadenylated RNAs recruited to our condensates. We previously assessed this strategy using ArtiG^{PUMilio} condensates and found that those condensates recruited polyadenylated RNAs (42). Here, we found that ArtiG$^{mCh/MCP/RNA}$ also displayed a strong coronal PABP-GFP signal, which was not observed around control ArtiG^{mCh} and ArtiG$^{mCh/MCP}$ (Fig. S2A). These data suggest that MCP does not significantly interact with other cellular polyadenylated RNAs than RNA-MS2, thus confirming the specificity of ArtiG$^{emGFP/MCP}$ for RNA-MS2. As an additional control, we verified by western blotting that the expression level of the scaffold proteins is not altered by the co-transfection of RNA-MS2 (Fig. S2B). When quantifying the total number of RNA-MS2 molecules dispersed in the cytoplasm and localized on ArtiG$^{emGFP/MCP}$, we found that 34% ± 19% of the cytoplasmic mRNAs were specifically recruited at the condensate surface (mean of 430 recruited RNAs and 1200 dispersed RNAs per cell) (Fig. 1F). Altogether, these data show that ArtiG$^{emGFP/MCP}$ act as condensates localizing specific RNAs on their surfaces (ArtiG$^{emGFP/MCP/RNA}$).

RNAs modify the material properties of ArtiG condensates

The observation that RNAs only localized to the surface and not within the core of the condensates could be a consequence of the specific material properties of the condensates. To further characterize this aspect, we performed fluorescence recovery after photobleaching experiments (FRAP) in cells expressing ArtiG condensates (ArtiG^{emGFP}, ArtiG$^{emGFP/MCP}$ without and with RNA-MS2 expression). In ArtiG^{emGFP} condensates, about 43% of the signal recovered with a half-recovery time of about 7 seconds (Fig. 2A-B). This time-scale reflects binding/unbinding states of the mobile fraction of the condensed phase, which dynamically exchanges with the cytosolic diluted phase. ArtiG$^{emGFP/MCP}$ (without RNA-MS2 transfection) displayed a reduced recovery amplitude with a signal that kept slowly increasing over 2 min without completely reaching a plateau, indicating that the mobile fraction reorganized and continuously exchanged with the cytosol at a minute scale. This indicates that MCP proteins increased the condensate viscosity (Fig. 2A-B). In contrast, in the presence of RNA-MS2, ArtiG$^{emGFP/MCP/RNA}$ recovery rapidly reached a plateau regime corresponding to about 20% recovery. The initial fast recovery of those ArtiG$^{emGFP/MCP/RNA}$ lasted less than 1s in most FRAP experiments, reflecting the rapid diffusion of the protein scaffold. Overall, the recovery curves of ArtiG$^{emGFP/MCP}$ with RNA are typical of gel-like phases, with the RNA-MS2 inducing a hardening of the condensate (Fig. 2A-B). This hardening could in turn explain why RNA-MS2 molecules remain at condensate surface.

Cytosolic target RNAs are depleted at the vicinity of large condensates

As our data showed a robust recruitment of RNAs at the surface of ArtiG$^{emGFP/MCP}$ condensates, we next investigated whether this recruitment impacted the distribution of RNAs in the cytoplasm. Interestingly, we observed a depletion of cytoplasmic MS2-RNAs close to ArtiG$^{emGFP/MCP/RNA}$ condensates (Fig. 2C and Fig. S3A). This depletion was readily visible around large condensate clusters recruiting a high number of RNA molecules. On the examples shown in Fig. 2C and Fig. S3A, we quantified the density of RNAs as a function of the distance to the condensate edges. RNA density was almost zero in a large area ranging from the immediate vicinity of the cluster up to 3 µm from the condensate border. Then, RNA density increased until reaching a plateau at a distance of about 4 µm, with a value corresponding to the mean cytoplasmic RNA concentration of the cell (Fig. 2D, red dots, and Fig. S3B). The values over the plateau (Fig. 2D, empty red dots) result from the analyzed area occasionally including neighbouring condensates. Likewise, plotting the cumulative number of RNAs outside the condensates as a function of the distance to the condensate edges showed first a very slow increase up to 3 µm from the condensate edges (Fig. 2E, red dots, and Fig S3C). Beyond this depletion area, the increase sharpened with a steady slope corresponding to an even cytoplasmic RNA concentration, except when including neighbouring condensates (Fig. 2E, empty red dots). For comparison, we quantified the spatial distribution of ß-actin mRNAs, which do not bind to ArtiG^{MCP}. We found a total absence of depletion of ß-actin mRNAs around ArtiG clusters (Fig. 2F), with an even RNA density around the condensates (Fig. 2D and E, violet dots). Altogether, these results suggest that the RNA depletion was linked to the specific recruitment of RNA-MS2 on condensates rather than from potential non-specific steric exclusion at the vicinity of condensates.

Artificial condensates are biochemically distinct from endogenous condensates

In a cellular context, biologically distinct RNP condensates that form in the same cytoplasm can interact with each other through shared proteins and RNAs, as described for P-bodies (PBs) and stress granules (SGs) (53) or PBs and U-bodies (54). Therefore, we next sought to investigate whether the local enrichment of mRNAs on ArtiG$^{emGFP/MCP}$ may induce interactions with other cytoplasmic RNP granules. To this aim, we looked at the presence of PBs by immunostaining 24 h after transfection, using DDX6 as a PB marker. Our observations showed no particular physical proximity or docking between the two condensates (Fig. 3A, left panel). Similarly, there was no proximity between ArtiG$^{emGFP/MCP}$ and SGs, using ATXN2L as a SG marker (Fig. S4A). Moreover, no docking of ArtiG$^{emGFP/MCP/RNA}$ with SGs was observed after SG induction with an arsenite stress (Fig. 3A,

right panel). These results suggest that ArtiG$^{emGFP/MCP/RNA}$ are biochemically distinct and physically independent from both PBs and SGs**.**

Controlled dissolution of artificial condensates

Recent studies suggest that the formation and stability of biological condensates are tightly regulated by multiple stimuli, including post-translational modifications, biochemical reactions, or physical parameters such as temperature or osmotic pressure changes (55, 56). By design, the formation and stability of the ArtiG$^{emGFP/MCP}$ condensates are driven by multivalent interactions mediated by the Fm-Fm homodimer, and these interactions could in principle be disrupted by the addition of a chemical competitor, FK506 (52). We therefore assessed if FK506 addition could first prevent condensate formation and secondly dissolve already formed condensates (Fig. 3B). In the absence of FK506, the majority of transfected cells exhibited ArtiG$^{emGFP/MCP/RNA}$ condensates (93% after 24 h of expression, Fig. 3C). This percentage dropped to 15% upon addition of FK506 at the time of transfection, with the majority of cells displaying a diffuse emGFP fluorescence and a homogeneous MS2-RNA distribution in the cytosol (Fig. 3D). Thus, FK506 efficiently inhibited the formation of the condensates. In a second experimental design, we examined the dissolution of fully formed ArtiGs by adding FK506 24 h after transfection (Fig. 3B). After 2 h of FK506 incubation, we found that the majority of cells lacked ArtiGs and displayed diffuse emGFP with Cy3-labelled MS2-RNAs distributed throughout the cytoplasm (70%, Fig. 3C). Thus, FK506 treatment induced the dissolution of the majority of pre-formed ArtiG$^{emGFP/MCP/RNA}$ condensates. To further characterize FK506 effect, we examined the time-scale of dissolution using live confocal microscopy. Upon addition of FK506, some cells exhibited condensates dissolving within few seconds (Fig. 3E), while in others dissolution took up to 30 minutes (Fig. S4B). These dissolutions were accompanied with a strong increase of the cytosolic fluorescence signal, corresponding to the release of the ArtiG scaffold (Fig. 3F). We also observed a few cells with smaller condensates and a stronger cytosolic fluorescence, corresponding to incomplete condensate dissolution, in agreement with the observation of residual condensates in fixed cells (Fig. S4C). Altogether, our data showed that pre-treatment with the FK506 binding competitor of Fm proteins provides a mean of preventing the formation of the ArtiG condensates, while it globally induces their disassembly when they are already formed. Our system thus allows for a controlled inhibition and disassembly (by adding FK506) of artificial condensates in living cells.

Linking condensate size and number of recruited RNAs

Determining how the primary constituents of condensates set the variety of condensate size and morphology naturally observed in cells remains very complex, since RNAs and proteins establish

a large network of interactions. The ArtiG condensates potentially provide an important simplification to this problem, as only one RNA species is recruited to the condensates. We could therefore analyze how RNA contributes to ArtiG$^{emGFP/MCP/RNA}$ condensate morphology, by quantifying the recruitment of MS2-RNAs in condensates and condensate size in each cell. Within the same transfection experiment, the size and number of ArtiG$^{emGFP/MCP/RNA}$ condensates were heterogenous between cells, with some cells exhibiting few condensates and others a larger number (Fig. 4A). The distribution of the mean diameter of ArtiG condensates roughly ranged from 0.4 to 4 µm depending on the cell (mean ± SD = 1.1 ± 0.6 µm, coefficient of variation CV = 58%, Fig. 4B, left panel). While 75% of the cells had condensates with a mean diameter below 1.5 µm, we observed particularly large condensates, up to 4 µm in diameter, in the other cells. The number of condensates per cell was also very diverse (mean number = 33, CV = 116%, Fig. 4B, right panel). Interestingly, condensate mean size per cell was inversely related to their number (Fig. 4C). Indeed, cells displaying large condensates (diameter > 1.5 µm) always had a limited number of them (< 25). In contrast, a higher number of condensates in a cell (> 25) was correlated with a mean diameter of the condensates below 1.5 µm. In contrast to the heterogeneity of condensate size between cells, we found a homogeneity of size within a given cell (average CV=30%, Fig. 4D).

We next sought to examine whether there was a correlation between condensate number and size, and RNA recruitment. To this aim, we computed, per cell, the density of RNAs recruited at the surface of ArtiG condensates and their mean diameter (Fig. 4E). We could highlight two groups of cells. In cells displaying large condensates (mean diameter > 1.5 µm, mean ± SD = 2.0 ± 0.6 µm), the RNA surface density was below 5 RNAs/µm² (mean = 2.0 RNAs/µm², Fig. 4E, green dots). These condensates were generally spherical with a small number of RNAs at their periphery. In contrast, a higher RNA density (> 5 RNAs/µm², mean = 16.0 RNA/µm²) was associated with a mean diameter of ArtiG below 1.5 µm (mean ± SD = 0.79 ± 0.32 µm, Fig. 4E, orange dots). In these cells, condensates were often found in close proximity to each other, forming cluster-like patterns (more than 5 condensates docking together) with RNA patches or corona separating individual condensates (Fig. 4F). These clusters were reminiscent of coalescence events but their high number suggested that the coalescence process was arrested, so that condensates did not relax into a sphere. We even observed a few cases where ArtiG$^{emGFP/MCP}$ and RNA molecules seemed intertwined, with frontiers between condensates becoming blurred and ArtiG$^{emGFP/MCP/RNA}$ losing their round shape (Fig. 4G). To sum up, we found that all large spherical ArtiG condensates displayed few RNA molecules on their surfaces, while condensates with a high RNA surface density had a smaller size.

Evolution of condensate size and morphology as a function of RNA surface density

To refine our analysis of the role of RNA localization in the condensate morphology, we increased the expression of transcribed RNA-MS2 by transfecting a larger quantity of plasmids in cells (five-fold more, i.e. 250 ng). In this condition (RNA high) the mean number of RNA-MS2 transcripts per cell rose from about 1200 to around 2400, without affecting the expression of the ArtiG scaffold (Fig. S2b). The mean number of RNA-MS2 recruited at the surface of the condensates rose from 430 to 1100 (Fig. 5A, left panel). This was accompanied with changes in the condensate morphology. Firstly, the size of the condensates was drastically reduced as compared to the RNA low condition (0.72 ± 0.32 µm instead of 1.26 ± 0.68 µm), and even more as compared to conditions without RNA (Fig. 5A, middle and right panels). This result is in line with our observation that higher RNA surface localization resulted in smaller condensates. Furthermore, in the RNA high condition, very few cells displayed large condensates (diameter > 1.5 µm) (Fig. 5B) while the incidence of cluster-like patterns was much higher: about 64% of cells in regard to 43% in the RNA low condition and 35% in the no RNA condition (Fig. 5C). Among the clusters, condensate intertwining, which was a rare event in the low RNA condition (3.6%) and no RNA condition (4.6%), became more common (19%). Altogether these data confirm a direct relationship between RNA surface density and condensate size and number.

DISCUSSION

RNA is more and more recognized as a driving force in cellular organization and functions. These polymers can interact and scaffold hundreds of proteins to generate high order organizations including RNP condensates. The first high throughput biochemical studies of RNP condensates showed that their RNA and protein content is highly complex (57–60). While these studies highlight that condensation is driven by the combination of multiple RNA-protein, protein-protein, and RNA-RNA interactions, the rules governing RNA and protein spatiotemporal co-assembly are still enigmatic. As a consequence, deciphering and manipulating RNP condensates *in cellulo* remains a difficult task. In this context, *in vitro* reconstitution using purified components has been a powerful strategy (11, 22, 25, 61, 62). Physicochemical parameters defining RNA polymers such as their length, chemical complexity and sequence, could thus be assessed in a reconstituted environment. Despite their obvious advantages, several limitations arose from these reductionist approaches. For instance, the physiological relevance of the protein concentration used in *in vitro* model condensates and their minimal composition can be questioned, as well as their simplified physicochemical environment compared to cells. Alternatively, the over-expression of recombinant proteins, often

chosen among scaffolding proteins found to drive LLPS in test tube, was also widely used to identify the propensity of specific protein domains to undergo phase separation in a cellular environment (19, 63, 64). Complementary to these approaches, building RNP condensate mimics in cells using artificial condensates functionalized with a specific RBP (TIA-1, G3BP, or Pumilio) can be instrumental to establish a link between condensate biochemical functions and their material states, as illustrated by studies recapitulating the formation of physiological or pathological RNP condensates in cells (30, 31, 40, 42). However, even with such engineered condensates, untangling the specific role of RNA from the large complex network of RBP-RNA interactions at work during condensate formation remains challenging (65–67). To overcome this limitation, our approach was to reconstitute in cells artificial RNP condensates recruiting a single RNA species, thus providing a unique system to question the link between RNA recruitment and condensate size.

Remarkably, the recruited RNA molecules localized at the condensate surface, with two distinct patterns, either disperse or forming a corona around the condensates (Fig. 1 and S1). How these patterns emerge from the interactions between ArtiG^{MCP} scaffolds and MS2-RNAs? Several *in vitro* studies and numerical simulations reported how multilayered organizations, such as core-shell droplets, assemble from ternary systems composed of protein-RNA interacting molecules (22, 25, 26, 68–70). A possible mode of formation of these multiphase droplets results from competing intermolecular interactions between macromolecular constituents that drive differences in surface tension and coexisting liquid phases. In this regard, our RNP condensates differ from co-existing liquid phases that demix into core-shell droplets, since they generally displayed a single RNA molecule layer as a shell enveloping ArtiG condensates. Instead, the assembly pathway controlling the formation of condensates with an RNA corona could arise from a stepwise process: first, ArtiG^{MCP} scaffolds undergo LLPS and, subsequently, RNA molecules are recruited on the condensate surface, reaching a density that depends on the RNA expression level (Fig 5D). Interestingly, the recruitment of RNA also changed the material properties of ArtiG$^{MCP/RNA}$, by hardening the condensate body, which can also explain why RNA-MS2 molecules remain at their surface (Fig. 2A and B).

The robust formation of ArtiG condensates in cells provides a unique mean to examine basic questions such as how condensate size scales with RNA surface density. Indeed, the ability to count the RNA molecules recruited on ArtiGs allowed us to show that the RNA density at the surface of condensates was correlated to their size and number, with large condensates displaying only a few RNAs on their surface whereas high RNA density always implied smaller and more numerous condensates. Furthermore, when we increased RNA expression in cells, and consequently RNA surface density on condensates, cells harboured smaller condensates, which supports a causal relationship between RNA surface density and condensate size.

Several examples in cell biology suggest the existence of a scaling of cellular organelles with cell volume, which could be understood if cells contain a limiting pool of structural components supporting the organelle assembly (9, 71, 72). In cells, native condensates such as PBs and PML nuclear bodies are generally found as sub-micrometric bodies that often do not grow over a certain size. This is generally in contradiction with the thermodynamical equilibrium picture of phase separated systems predicting an evolution towards a single condensed phase co-existing with a dilute phase. Initial growth of phase-separated condensates generally occurs through subunit addition, and coarsening through coalescence or Ostwald ripening (73–75). Thus, a solution to regulate condensate size would be to tune one of these three pathways (subunit addition, coalescence and Ostwald ripening), either through physicochemical parameters or by modifying interaction strengths and valences by biochemical reactions such as post-translational modifications (76, 77). Recent theoretical studies suggest that both active and passive processes can be in play (78, 79). For instance, it has been proposed that active processes within condensates could suppress Ostwald ripening and account for size selection (71, 80–83). However, in the case of ArtiG$^{emGFP/MCP/RNA}$, the two main formation pathways are subunit addition and coalescence (Fig. 1B). Client proteins acting like surfactants may reduce the energy required for the formation of an interface between the dense and dilute phase and lead to size-conserved multi-droplet systems instead of the expected single large condensed phase, with condensate size decreasing as a result of client concentration increasing (84) In this respect, the protein Ki-67, localized at the surface of chromosomes, may for instance form a steric barrier that prevents the chromosomes from collapsing into a single entity (85). A high surface charge density and thus a high electrostatic repulsion between biomolecular condensates may alter their propensity to fuse (86). *In vitro* observations of the co-assembly between RNA homopolymers and mRNAs showed multi-phase assemblies, with RNAs localized at the droplet surface, suggesting that RNAs act as an interfacial shell stabilizing multiphase condensates (61). Thus, the biochemical and structural heterogeneity at the surface of condensates could also influence their stability. For instance in *C.elegans*, the adsorption of MEG-3 on PGL droplets drives the formation of a gel-like shell around a liquid core that eventually can stabilize P granules and trap RNAs (87, 88). More precisely, MEG-3 clusters on P granules have been shown recently to behave like Pickering agents decreasing the surface tension of the P granules, slowing down their coarsening (89). These results remind us of our observations with ArtiGranules fused to Pumilio, as we showed that PBs docking at the surface of the condensates impacted their formation (42). Alternatively, a recent study explained how the RNA shell-forming domain of paraspeckles can modulate condensate shape and size and suggested a micellization-based model of assembly (90). Here we propose that the RNA present at the surface of ArtiG condensates cause a steric hindrance that may prevent the growth of condensates by both subunit addition and coalescence (Fig. 5D). Additionally, the hardening of the condensate

due to the presence of RNA could favor the arrested coalescence of the bodies and thus contribute to limit their growth during coarsening (Fig. 5D). In this picture, RNAs, through their charges and length, could contribute to the colloidal stability of the condensates and thus regulate their size and number.

At a high RNA surface density, we found that ArtiG condensates can lose their sphericity and adopt a clustered morphology reminiscent of TIS granules (24). However, in contrast to TIS granules, where a skeleton made of RNA-RNA interactions between unstructured regions counterbalances the excess of surface energy generally driving fusion and relaxation, here RNAs at the condensate surface could impede coalescence by steric hindrance. We could also envision the existence of intermolecular interactions between RNAs that would bridge adjacent ArtiG condensates and enhance their stability.

Such an impact of surface RNA on condensate morphology may be relevant for native RNP condensates. Indeed, the spatiotemporal organization of RNAs at the surface of native condensates has recently been investigated using advanced imaging tools. For example, super-resolution imaging showed that the solid core of SGs is surrounded by a less concentrated RNA and protein layer (60, 91). It has also been shown that RNAs exhibit diverse localization within PBs and at their surface (92). On SG or PB surface, RNAs can make transient contacts before stably associating inside the granules or leaving the granules for an alternative fate (92, 93). Some of these RNAs are coding mRNAs, thus associating with ribosomes and other translation-related proteins when not in granules (94), while others are long non-coding RNAs with a regulatory function (92). These RNAs can partition bidirectionally between biologically different condensates (93, 95). In the case of germ PBs, the association of the RNAs with the surface of the condensates can even be required for translation to happen (96). Along this line, our work suggests that localization of RNAs at the condensate surface could also feedback on condensate biogenesis.

In conclusion, our methodology to reconstitute biomolecular condensates in cells with controlled compositions and properties has proved powerful to reveal the role of surface RNA in condensate morphology and material properties. More generally, our study stresses the importance of an understudied aspect of condensates, which is the role of the biomolecules present at their surface, whether RNA or proteins. It illustrates how chemical and physical heterogeneities on condensate surface may determine granule morphology properties. Beyond this advance in the understanding of RNP condensate sizing, ArtiG-MCPs provide a powerful system, capable of recruiting any RNA of interest tagged with MS2. In addition, they can be chemically controlled to trigger their dissolution as well as to prevent their formation on demand. Due to its flexibility, we anticipate that our methodology will not only enable to address other basic biological issues in the future, but also be a mean to engineer novel properties within cells.

Data availability

All data are available from the corresponding author upon request.

Acknowledgments

The authors acknowledge all the members of the Biophysical Chemistry group of the École normale supérieure for fruitful discussion. We thank A. Imbert, M.A Plamont, M. Ernoult-Lange, M.N Benassy, M. Bénard, H. Saito, and S. Matsumoto for their help along the project, as well as Adham Safieddine for carefully reading the manuscript.

Funding

A.C was supported by IPV-SU PhD fellowship and ARC fellowship (ARCDOC42021020003470). M.G.J.N was supported by FRM (ING20150532742). This work was supported by the CNRS, Ecole Normale Supérieure, and ARC (20181208003) to Z.G., FRM (MND202003011470) and iBio (SU) to Z.G and D.W, and ANR (ANR-19-CE12-0024-01) to D.W.

Author Contributions

A.C, D.W and Z.G conceived the project and analyzed results. A.C carried out and analyzed most experiments. M.G.J.N contributed to the design of protein scaffolds and performed initial experiments. L.P performed FRAP experiments and analysis. S.K and M.K contributed to the design of synthetic RNAs. A.C, D.W and Z.G wrote the manuscript and all authors were involved in revising it critically for important intellectual content.

Declaration of Interests

The authors declare that they have no competing interests.

Supporting Information

4 supplementary figures and 1 supplementary table.

References:

1. Buchan,J.R. (2014) mRNP granules. *RNA Biology*, **11**, 1019–1030.

2. Brangwynne,C.P., Eckmann,C.R., Courson,D.S., Rybarska,A., Hoege,C., Gharakhani,J., Julicher,F. and Hyman,A.A. (2009) Germline P Granules Are Liquid Droplets That Localize by Controlled Dissolution/Condensation. *Science*, **324**, 1729–1732.

3. Li,P., Banjade,S., Cheng,H.-C., Kim,S., Chen,B., Guo,L., Llaguno,M., Hollingsworth,J. v., King,D.S., Banani,S.F., *et al.* (2012) Phase transitions in the assembly of multivalent signalling proteins. *Nature*, **483**, 336–340.

4. Shin,Y. and Brangwynne,C.P. (2017) Liquid phase condensation in cell physiology and disease. *Science*, **357**.

5. Boeynaems,S., Alberti,S., Fawzi,N.L., Mittag,T., Polymenidou,M., Rousseau,F., Schymkowitz,J., Shorter,J., Wolozin,B., Van,L., *et al.* (2018) Protein Phase Separation: A New Phase in Cell Biology. *Trends in Cell Biology*, **28**.

6. Banani,S.F., Lee,H.O., Hyman,A.A. and Rosen,M.K. (2017) Biomolecular condensates: organizers of cellular biochemistry. *Nature Reviews Molecular Cell Biology*, **18**, 285–298.

7. Standart,N. and Weil,D. (2018) P-Bodies: Cytosolic Droplets for Coordinated mRNA Storage. *Trends in Genetics*, **34**.

8. Lallemand-Breitenbach,V. and de Thé,H. (2010) PML nuclear bodies. *Cold Spring Harbor perspectives in biology*, **2**.

9. Decker,M., Jaensch,S., Pozniakovsky,A., Zinke,A., O'Connell,K.F., Zachariae,W., Myers,E. and Hyman,A.A. (2011) Limiting amounts of centrosome material set centrosome size in C. elegans embryos. *Current Biology*, **21**, 1259–1267.

10. Strom,A.R. and Brangwynne,C.P. (2019) The liquid nucleome – phase transitions in the nucleus at a glance. *Journal of Cell Science*, **132**, jcs235093.

11. Roden,C. and Gladfelter,A.S. (2020) RNA contributions to the form and function of biomolecular condensates. *Nature Reviews Molecular Cell Biology*, 10.1038/s41580-020-0264-6.

12. Shevtsov,S.P. and Dundr,M. (2011) Nucleation of nuclear bodies by RNA. *nature cell biology*, **13**, 167–173.

13. Schwartz,J.C., Wang,X., Podell,E.R. and Cech,T.R. (2013) RNA Seeds Higher-Order Assembly of FUS Protein. *Cell Reports*, **5**, 918–925.

14. Jain,A. and Vale,R.D. (2017) RNA phase transitions in repeat expansion disorders. *Nature*, **546**, 243–247.

15. Yamazaki,T., Souquere,S., Chujo,T., Nakagawa,S., Pierron,G., Correspondence,T.H., Kobelke,S., Chong,Y.S., Fox,A.H., Bond,C.S., *et al.* (2018) Functional Domains of NEAT1 Architectural lncRNA Induce Paraspeckle Assembly through Phase Separation Molecular Cell Article Functional Domains of NEAT1 Architectural lncRNA Induce Paraspeckle Assembly through Phase Separation. *Molecular Cell*, **70**, 1038–1053.

16. Saha,S., Weber,C.A., Nousch,M., Adame-Arana,O., Hoege,C., Hein,M.Y., Osborne-Nishimura,E., Mahamid,J., Jahnel,M., Jawerth,L., *et al.* (2016) Polar Positioning of Phase-Separated Liquid Compartments in Cells Regulated by an mRNA Competition Mechanism. *Cell*, **166**, 1572-1584.e16.

17. Falahati,H., Pelham-Webb,B., Blythe,S. and Wieschaus,E. (2016) Nucleation by rRNA dictates the precision of nucleolus assembly. *Current Biology*, **26**, 277–285.

18. Banerjee,P.R., Milin,A.N., Moosa,M.M., Onuchic,P.L. and Deniz,A.A. (2017) Reentrant Phase Transition Drives Dynamic Substructure Formation in Ribonucleoprotein Droplets. *Angewandte Chemie - International Edition*, **56**, 11354–11359.

19. Maharana,S., Wang,J., Papadopoulos,D.K., Richter,D., Pozniakovsky,A., Poser,I., Bickle,M., Rizk,S., Guillén-Boixet,J., Franzmann,T.M., *et al.* (2018) RNA buffers the phase separation behavior of prion-like RNA binding proteins. *Science*, **360**, 918–921.

20. Zhang,H., Elbaum-Garfinkle,S., Langdon,E.M., Taylor,N., Occhipinti,P., Bridges,A.A., Brangwynne,C.P. and Gladfelter,A.S. (2015) RNA Controls PolyQ Protein Phase Transitions. *Molecular Cell*, **60**, 220–230.

21. Elbaum-Garfinkle,S., Kim,Y., Szczepaniak,K., Chen,C.C.H., Eckmann,C.R., Myong,S. and Brangwynne,C.P. (2015) The disordered P granule protein LAF-1 drives phase separation into droplets with tunable viscosity and dynamics. *Proceedings of the National Academy of Sciences of the United States of America*, **112**, 7189–7194.

22. Boeynaems,S., Holehouse,A.S., Weinhardt,V., Kovacs,D., Lindt,J. van, Larabell,C., Van,L., Bosch,D., Das,R., Tompa,P.S., *et al.* (2019) Spontaneous driving forces give rise to protein−RNA condensates with coexisting phases and complex material properties. *PNAS*, **116**.

23. Langdon,E.M., Qiu,Y., Ghanbari Niaki,A., McLaughlin,G.A., Weidmann,C., Gerbich,T.M., Smith,J.A., Crutchley,J.M., Termini,C.M., Weeks,K.M., *et al.* (2018) mRNA structure determines specificity of a polyQ-driven phase separation. *Science*, **360**, 922–927.

24. Ma,W., Zheng,G., Xie,W. and Mayr,C. (2021) In vivo reconstitution finds multivalent RNA–RNA interactions as drivers of mesh-like condensates. *eLife*, **10**.

25. Kaur,T., Raju,M., Alshareedah,I., Davis,R.B., Potoyan,D.A. and Banerjee,P.R. (2021) Sequence-encoded and composition-dependent protein-RNA interactions control multiphasic condensate morphologies. *Nature Communications*, **12**, 872.

26. Feric,M., Vaidya,N., Harmon,T.S., Mitrea,D.M., Zhu,L., Richardson,T.M., Kriwacki,R.W., Pappu,R. v. and Brangwynne,C.P. (2016) Coexisting Liquid Phases Underlie Nucleolar Subcompartments. *Cell*, **165**, 1686–1697.

27. Snead,W.T., Gerbich,T.M., Seim,I., Hu,Z. and Gladfelter,A.S. (2021) Membrane surfaces regulate assembly of a ribonucleoprotein condensate. *bioRxiv*, 10.1101/2021.04.24.441251.

28. Feric,M., Brangwynne,C.P., Cell,N. and Author,B. (2013) A nuclear F-actin scaffold stabilizes RNP droplets against gravity in large cells HHS Public Access Author manuscript. *Nat Cell Biol*, **15**, 1253–1259.

29. Lee,D.S.W., Wingreen,N.S. and Brangwynne,C.P. (2021) Chromatin mechanics dictates subdiffusion and coarsening dynamics of embedded condensates. *Nature Physics*, **17**, 531–538.

30. Shin,Y., Berry,J., Pannucci,N., Haataja,M.P., Toettcher,J.E. and Brangwynne,C.P. (2017) Spatiotemporal Control of Intracellular Phase Transitions Using Light-Activated optoDroplets. *Cell*, **168**, 159-171.e14.

31. Mann,J.R., Gleixner,A.M., Mauna,J.C., Gomes,E., DeChellis-Marks,M.R., Needham,P.G., Copley,K.E., Hurtle,B., Portz,B., Pyles,N.J., *et al.* (2019) RNA Binding Antagonizes Neurotoxic Phase Transitions of TDP-43. *Neuron*, **102**, 321-338.e8.

32. Watanabe,T., Seki,T., Fukano,T., Sakaue-Sawano,A., Karasawa,S., Kubota,M., Kurokawa,H., Inoue,K., Akatsuka,J. and Miyawaki,A. (2017) Genetic visualization of protein interactions harnessing liquid phase transitions. *Scientific Reports*, **7**, 1–13.

33. Bracha,D., Walls,M.T., Wei,M.-T., Avalos,J.L., Toettcher,J.E., Correspondence,C.P.B., Zhu,L., Kurian,M. and Brangwynne,C.P. (2018) Mapping Local and Global Liquid Phase Behavior in Living Cells Using Photo-Oligomerizable Seeds. *Cell*, **175**, 1467–1480.

34. Schuster,B.S., Reed,E.H., Parthasarathy,R., Jahnke,C.N., Caldwell,R.M., Bermudez,J.G., Ramage,H., Good,M.C. and Hammer,D.A. (2018) Controllable protein phase separation and modular recruitment to form responsive membraneless organelles. *Nature Communications*, **9**, 1–12.

35. Reinkemeier,C.D., Estrada Girona,G. and Lemke,E.A. (2019) Designer membraneless organelles enable codon reassignment of selected mRNAs in eukaryotes. *Science*, **363**.

36. Dzuricky,M., Rogers,B.A., Shahid,A., Cremer,P.S. and Chilkoti,A. (2020) De novo engineering of intracellular condensates using artificial disordered proteins. *Nature Chemistry*, **12**, 814–825.

37. Heidenreich,M., Georgeson,J.M., Locatelli,E., Rovigatti,L., Nandi,S.K., Steinberg,A., Nadav,Y., Shimoni,E., Safran,S.A., Doye,J.P.K., *et al.* (2020) Designer protein assemblies with tunable phase diagrams in living cells. *Nature Chemical Biology*, **16**, 939–945.

38. Yoshikawa,M., Yoshii,T., Ikuta,M. and Tsukiji,S. (2021) Synthetic Protein Condensates That Inducibly Recruit and Release Protein Activity in Living Cells. *Journal of the American Chemical Society*, **143**, 6434–6446.

39. Lasker,K., Boeynaems,S., Lam,V., Stainton,E., Jacquemyn,M., Daelemans,D., Villa,E., Holehouse,A.S., Gitler,A.D. and Shapiro,L. (2021) A modular platform for engineering function of natural and synthetic biomolecular condensates. *bioRxiv*, 10.1101/2021.02.03.429226.

40. Nakamura,H., Lee,A.A., Afshar,A.S., Watanabe,S., Rho,E., Razavi,S., Suarez,A., Lin,Y.C., Tanigawa,M., Huang,B., *et al.* (2018) Intracellular production of hydrogels and synthetic RNA granules by multivalent molecular interactions. *Nature Materials*, **17**, 79–88.

41. Sanders,D.W., Kedersha,N., Lee,D.S.W., Strom,A.R., Drake,V., Riback,J.A., Bracha,D., Eeftens,J.M., Iwanicki,A., Wang,A., *et al.* (2020) Competing Protein-RNA Interaction Networks Control Multiphase Intracellular Organization. *Cell*, **181**, 306-324.e28.

42. Garcia-Jove Navarro,M., Kashida,S., Chouaib,R., Souquere,S., Pierron,G., Weil,D. and Gueroui,Z. (2019) RNA is a critical element for the sizing and the composition of phase-separated RNA–protein condensates. *Nature Communications*, **10**, 3230.

43. Coller,J.M., Gray,N.K. and Wickens,M.P. (1998) mRNA stabilization by poly(A) binding protein is independent of poly(A) and requires translation. *Genes & Development*, **12**, 3226–3235.

44. Wu,B., Chao,J.A. and Singer,R.H. (2012) Fluorescence fluctuation spectroscopy enables quantitative imaging of single mRNAs in living cells. *Biophysical Journal*, **102**, 2936–2944.

45. Strein,C., Alleaume,A.M., Rothbauer,U., Hentze,M.W. and Castello,A. (2014) A versatile assay for RNA-binding proteins in living cells. *RNA*, **20**, 721–731.

46. Tsanov,N., Samacoits,A., Chouaib,R., Traboulsi,A.-M., Gostan,T., Weber,C., Zimmer,C., Zibara,K., Walter,T., Peter,M., *et al.* (2016) smiFISH and FISH-quant – a flexible single RNA detection approach with super-resolution capability. *Nucleic Acids Research*, **44**, e165–e165.

47. Schindelin,J., Arganda-Carreras,I., Frise,E., Kaynig,V., Longair,M., Pietzsch,T., Preibisch,S., Rueden,C., Saalfeld,S., Schmid,B., *et al.* (2012) Fiji: An open-source platform for biological-image analysis. *Nature Methods*, **9**, 676–682.

48. de Chaumont,F., Dallongeville,S., Chenouard,N., Hervé,N., Pop,S., Provoost,T., Meas-Yedid,V., Pankajakshan,P., Lecomte,T., le Montagner,Y., *et al.* (2012) Icy: An open bioimage informatics platform for extended reproducible research. *Nature Methods*, **9**, 690–696.

49. Imbert,A., Ouyang,W., Safieddine,A., Coleno,E., Zimmer,C., Bertrand,E., Walter,T. and Mueller,F. (2021) FISH-quant v2: a scalable and modular analysis tool for smFISH image analysis. *bioRxiv*, 10.1101/2021.07.20.453024.

50. Olivo-Marin,J.-C. (2002) Extraction of spots in biological images using multiscale products.

51. Postma,M. and Goedhart,J. (2019) Plotsofdata—a web app for visualizing data together with their summaries. *PLoS Biology*, **17**, e3000202.

52. Rollins,C.T., Rivera,V.M., Woolfson,D.N., Keenan,T., Hatada,M., Adams,S.E., Andrade,L.J., Yaeger,D., van Schravendijk,M.R., Holt,D.A., *et al.* (2000) A ligand-reversible dimerization system for controlling protein-protein interactions. *Proceedings of the National Academy of Sciences of the United States of America*, **97**, 7096–101.

53. Wilczynska,A., Aigueperse,C., Kress,M., Dautry,F. and Weil,D. (2005) The translational regulator CPEB1 provides a link between dcp1 bodies and stress granules. *Journal of Cell Science*, **118**, 981–992.

54. Liu,J.L. and Gall,J.G. (2007) U bodies are cytoplasmic structures that contain uridine-rich small nuclear ribonucleoproteins and associate with P bodies. *Proceedings of the National Academy of Sciences of the United States of America*, **104**, 11655–11659.

55. Snead,W.T. and Gladfelter,A.S. (2019) The Control Centers of Biomolecular Phase Separation: How Membrane Surfaces, PTMs, and Active Processes Regulate Condensation. *Molecular Cell*, **76**, 295–305.

56. Jalihal,A.P., Schmidt,A., Gao,G., Little,S.R., Pitchiaya,S. and Walter,N.G. (2021) Hyperosmotic phase separation: Condensates beyond inclusions, granules and organelles. *Journal of Biological Chemistry*, **296**, 100044.

57. Saitoh,N., Spahr,C.S., Patterson,S.D., Bubulya,P., Neuwald,A.F. and Spector,D.L. (2004) Proteomic Analysis of Interchromatin Granule Clusters. *Molecular Biology of the Cell*, **15**, 3876–3890.

58. Hubstenberger,A., Courel,M., Bénard,M., Souquere,S., Ernoult-Lange,M., Chouaib,R., Yi,Z., Morlot,J.-B., Munier,A., Fradet,M., *et al.* (2017) P-Body Purification Reveals the Condensation of Repressed mRNA Regulons. *Molecular cell*, **68**, 144-157.e5.

59. Khong,A., Matheny,T., Jain,S., Mitchell,S.F., Wheeler,J.R. and Parker,R. (2017) The Stress Granule Transcriptome Reveals Principles of mRNA Accumulation in Stress Granules. *Molecular Cell*, **68**, 808-820.e5.

60. Jain,S., Wheeler,J.R., Walters,R.W., Agrawal,A., Barsic,A. and Correspondence,R.P. (2016) ATPase-Modulated Stress Granules Contain a Diverse Proteome and Substructure. *Cell*, **164**, 487–498.

61. Tauber,D., Tauber,G., Khong,A., van Treeck,B., Pelletier,J. and Parker,R. (2020) Modulation of RNA Condensation by the DEAD-Box Protein eIF4A. *Cell*, 10.1016/j.cell.2019.12.031.

62. Guillé N-Boixet,J., Kopach,A., Holehouse,A.S., Pappu,R. v, Alberti,S., Franzmann Correspondence,T.M., Wittmann,S., Jahnel,M., Schlü,R., Kim,K., *et al.* (2020) RNA-Induced Conformational Switching and Clustering of G3BP Drive Stress Granule Assembly by Condensation Article RNA-Induced

Conformational Switching and Clustering of G3BP Drive Stress Granule Assembly by Condensation. *Cell*, **181**, 346-361.e17.

63. Banani,S.F., Rice,A.M., Peeples,W.B., Lin,Y., Jain,S., Parker,R. and Rosen Correspondence,M.K. (2016) Compositional Control of Phase-Separated Cellular Bodies In Brief What are the general principles that define the composition of phase-separated cellular bodies? *Cell*, **166**, 651–663.

64. Nott,T.J., Petsalaki,E., Farber,P., Jervis,D., Fussner,E., Plochowietz,A., Craggs,T.D., Bazett-Jones,D.P., Pawson,T., Forman-Kay,J.D., *et al.* (2015) Phase Transition of a Disordered Nuage Protein Generates Environmentally Responsive Membraneless Organelles. *Molecular Cell*, **57**, 936–947.

65. van Treeck,B. and Parker,R. (2018) Emerging Roles for Intermolecular RNA-RNA Interactions in RNP Assemblies. *Cell*, **174**, 791–802.

66. Gomes,E. and Shorter,J. (2019) The molecular language of membraneless organelles. *Journal of Biological Chemistry*, **294**, 7115–7127.

67. Adekunle,D.A. and Hubstenberger,A. (2020) The multiscale and multiphase organization of the transcriptome. *Emerging Topics in Life Sciences*, **4**, 265–280.

68. Harmon,T.S., Holehouse,A.S. and Pappu,R. v. (2018) Differential solvation of intrinsically disordered linkers drives the formation of spatially organized droplets in ternary systems of linear multivalent proteins. *New Journal of Physics*, **20**, 045002.

69. Mountain,G.A. and Keating,C.D. (2020) Formation of Multiphase Complex Coacervates and Partitioning of Biomolecules within them. *Biomacromolecules*, **21**, 630–640.

70. Lu,T. and Spruijt,E. (2020) Multiphase Complex Coacervate Droplets. *Journal of the American Chemical Society*, **142**, 2905–2914.

71. Zwicker,D., Decker,M., Jaensch,S., Hyman,A.A. and Jülicher,F. (2014) Centrosomes are autocatalytic droplets of pericentriolar material organized by centrioles. *Proceedings of the National Academy of Sciences of the United States of America*, **111**, E2636–E2645.

72. Brangwynne,C.P. (2013) Phase transitions and size scaling of membrane-less organelles. *Journal of Cell Biology*, **203**, 875–881.

73. Berry,J., Weber,S.C., Vaidya,N., Haataja,M., Brangwynne,C.P. and Weitz,D.A. (2015) RNA transcription modulates phase transition-driven nuclear body assembly. *Proceedings of the National Academy of Sciences of the United States of America*, **112**, E5237–E5245.

74. Berry,J., Brangwynne,C.P. and Haataja,M. (2018) Physical principles of intracellular organization via active and passive phase transitions. *Reports on Progress in Physics*, **81**, 046601.

75. Brangwynne,C.P., Mitchison,T.J. and Hyman,A.A. (2011) Active liquid-like behavior of nucleoli determines their size and shape in Xenopus laevis oocytes. *Proceedings of the National Academy of Sciences of the United States of America*, **108**, 4334–9.

76. Söding,J., Zwicker,D., Sohrabi-Jahromi,S., Boehning,M. and Kirschbaum,J. (2019) Mechanisms for Active Regulation of Biomolecular Condensates Trends in Cell Biology. *Trends in Cell Biology*, 10.1016/j.tcb.2019.10.006.

77. Kirschbaum,J. and Zwicker,D. Controlling biomolecular condensates via chemical reactions.

78. Dar,F. and Pappu,R. (2020) Restricting the sizes of condensates. *eLife*, **9**, 1–3.

79. Ranganathan,S. and Shakhnovich,E.I. (2020) Dynamic metastable long-living droplets formed by sticker-spacer proteins. *eLife*, **9**, 1–25.

80. Weber,C.A., Zwicker,D., Jülicher,F. and Lee,C.F. (2019) Physics of active emulsions. *Reports on Progress in Physics*, **82**, 064601.

81. Zwicker,D., Hyman,A.A. and Jülicher,F. (2015) Suppression of Ostwald ripening in active emulsions. *PHYSICAL REVIEW E*, **92**, 12317.

82. Bressloff,P.C. (2020) Active suppression of Ostwald ripening: Beyond mean-field theory. *Physical Review E*, **101**, 42804.

83. David Wurtz,J. and Lee,C.F. (2018) Chemical-Reaction-Controlled Phase Separated Drops: Formation, Size Selection, and Coarsening. *Physical Review Letters*, **120**.

84. Sanchez-Burgos,I., Joseph,J.A., Collepardo-Guevara,R. and Espinosa,J.R. (2021) Size conservation emerges spontaneously in biomolecular condensates formed by scaffolds and surfactant clients. *bioRxiv*, 10.1101/2021.04.30.442154.

85. Cuylen,S., Blaukopf,C., Politi,A.Z., Muller-Reichert,T., Neumann,B., Poser,I., Ellenberg,J., Hyman,A.A. and Gerlich,D.W. (2016) Ki-67 acts as a biological surfactant to disperse mitotic chromosomes. *Nature*, **535**, 308–312.

86. Welsh,T.J., Krainer,G., Espinosa,J.R., Joseph,J.A., Sridhar,A., Jahnel,M., Arter,W.E., Saar,K.L., Alberti,S., Collepardo-Guevara,R., *et al.* (2022) Surface Electrostatics Govern the Emulsion Stability of Biomolecular Condensates. *Nano Letters*, **22**, 612–621.

87. Putnam,A., Cassani,M., Smith,J. and Seydoux,G. (2019) A gel phase promotes condensation of liquid P granules in Caenorhabditis elegans embryos. *Nature Structural & Molecular Biology*, **26**, 220–226.

88. Lee,C.Y.S., Putnam,A., Lu,T., He,S., Ouyang,J.P.T. and Seydoux,G. (2020) Recruitment of mRNAs to P granules by condensation with intrinsically-disordered proteins. *eLife*, **9**.

89. Folkmann,A.W., Putnam,A., Lee,C.F. and Seydoux,G. (2021) Regulation of biomolecular condensates by interfacial protein clusters. *Science*, **373**.

90. Yamazaki,T., Yamamoto,T., Yoshino,H., Souquere,S., Nakagawa,S., Pierron,G. and Hirose,T. (2021) Paraspeckles are constructed as block copolymer micelles. *The EMBO Journal*, **40**, e107270.

91. Wheeler,J.R., Matheny,T., Jain,S., Abrisch,R. and Parker,R. (2016) Distinct stages in stress granule assembly and disassembly. *eLife*, **5**.

92. Pitchiaya,S., Mourao,M.D.A., Jalihal,A.P., Xiao,L., Jiang,X., Chinnaiyan,A.M., Schnell,S. and Walter,N.G. (2019) Dynamic Recruitment of Single RNAs to Processing Bodies Depends on RNA Functionality. *Molecular Cell*, **74**, 521-533.e6.

93. Moon,S.L., Morisaki,T., Khong,A., Lyon,K., Parker,R. and Stasevich,T.J. (2019) Multicolour single-molecule tracking of mRNA interactions with RNP granules. *Nature Cell Biology*, **21**, 162–168.

94. Mateju,D., Eichenberger,B., Voigt,F., Eglinger,J., Roth,G. and Chao,J.A. (2020) Single-Molecule Imaging Reveals Translation of mRNAs Localized to Stress Granules. *Cell*, 10.1016/j.cell.2020.11.010.

95. Wilbertz,J.H., Voigt,F., Horvathova,I., Roth,G., Zhan,Y. and Chao,J.A. (2019) Single-Molecule Imaging of mRNA Localization and Regulation during the Integrated Stress Response. *Molecular Cell*, **73**, 946-958.e7.

96. Davidson,A., Parton,R.M., Rabouille,C., Weil,T.T. and Davis,I. (2016) Localized Translation of gurken/TGF-α mRNA during Axis Specification Is Controlled by Access to Orb/CPEB on Processing Bodies. *Cell Reports*, **14**, 2451–2462.

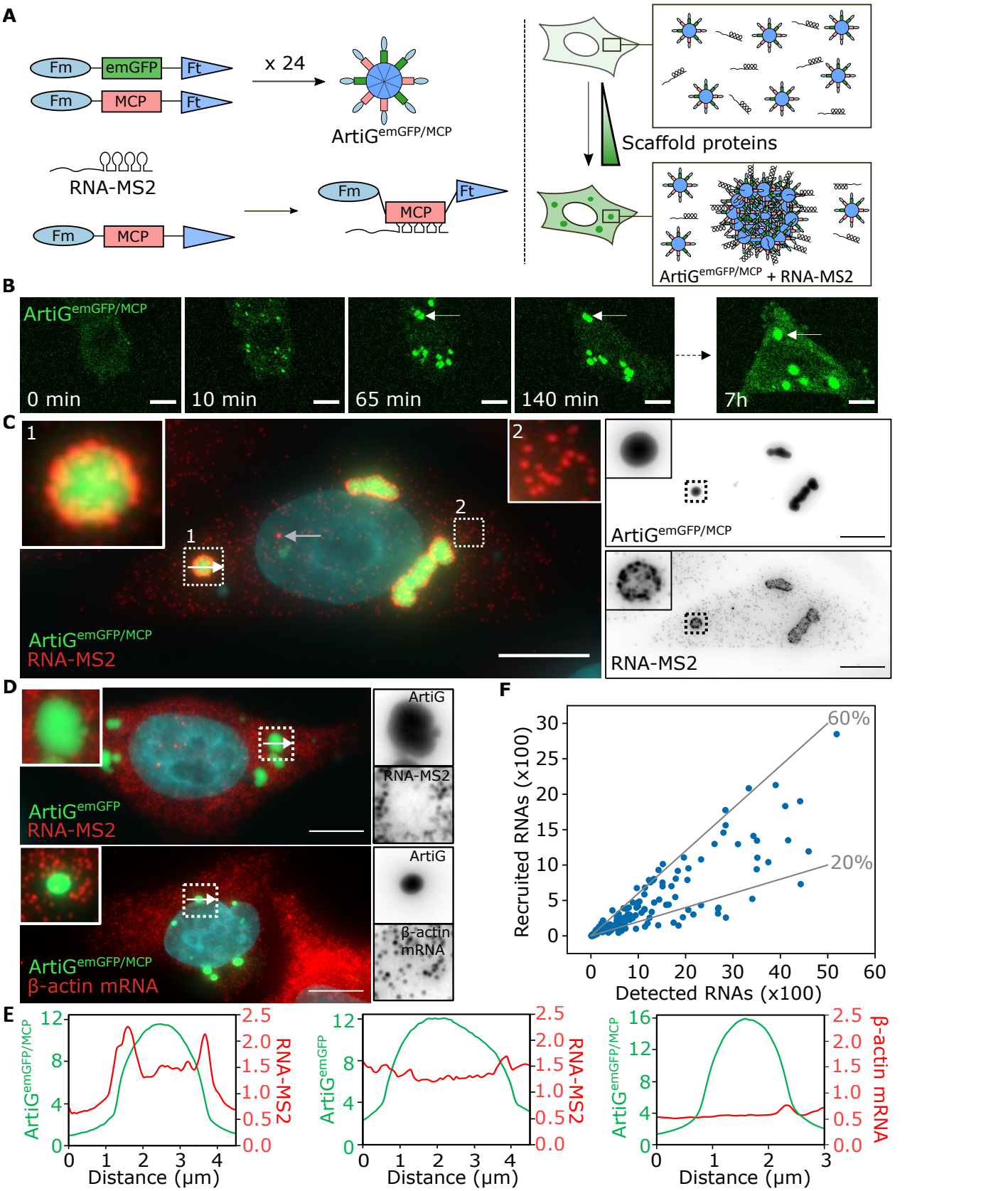

Figure 1: ArtiG^{MCP} condensates recruit a specific exogenous RNA. **A.** Schematic of the ArtiG$^{emGFP/MCP}$ formation (Fm = F36M-FKBP, MCP = MS2 coat protein, Ft = Ferritin, ArtiG = ArtiGranule). ArtiG$^{emGFP/MCP}$ form by LLPS driven by the homodimerization of Fm around Ferritin nanocages. MCP protein enable the recruitment of RNA-MS2 molecules to the condensates. **B.** Time-lapse confocal imaging of the formation of ArtiG$^{emGFP/MCP}$ in Hela cells starting 8 hours after transfection with plasmids Fm-emGFP-Ft and Fm-MCP-Ft (1:1 plasmid ratio). The white arrow highlights a coalescence event. Scale bar = 10 μm. **C.** Epifluorescence imaging of ArtiG$^{emGFP/MCP}$ (green) and RNA-MS2 (red). Cells were fixed 24 h after transfection of scaffold and RNA-MS2 plasmids (low RNA condition in the methods, i.e. 50 ng RNA-MS2). Nuclei were stained with DAPI (blue in merge). The zoom in insert 1 shows the recruitment of RNA-MS2 around an ArtiG$^{emGFP/MCP}$ condensate. Insert 2 shows isolated RNA-MS2 molecules. The white arrow indicates where the intensity profile in **E.** (left panel) was plotted. The grey arrow highlights a transcription focus. On the right panel, greyscale images correspond to separate channels. Scale bar = 10 μm. **D.** Epifluorescence imaging of ArtiG^{emGFP} (green) and RNA-MS2 (upper panel) or β-actin mRNA (lower panel) (red). The white arrows indicate where the intensity profiles in **E.** (middle and right panels) were plotted. Scale bar = 10 μm. **E.** Intensity profiles across ArtiG condensates (white arrows in **C** and **D**). **F.** Number of RNA-MS2 molecules recruited at the surface of ArtiG$^{emGFP/MCP}$ as a function of the total number of molecules detected in the cell, with each dot representing one cell (N = 140 from two independent experiments). Grey lines represent 20% and 60% recruitment.

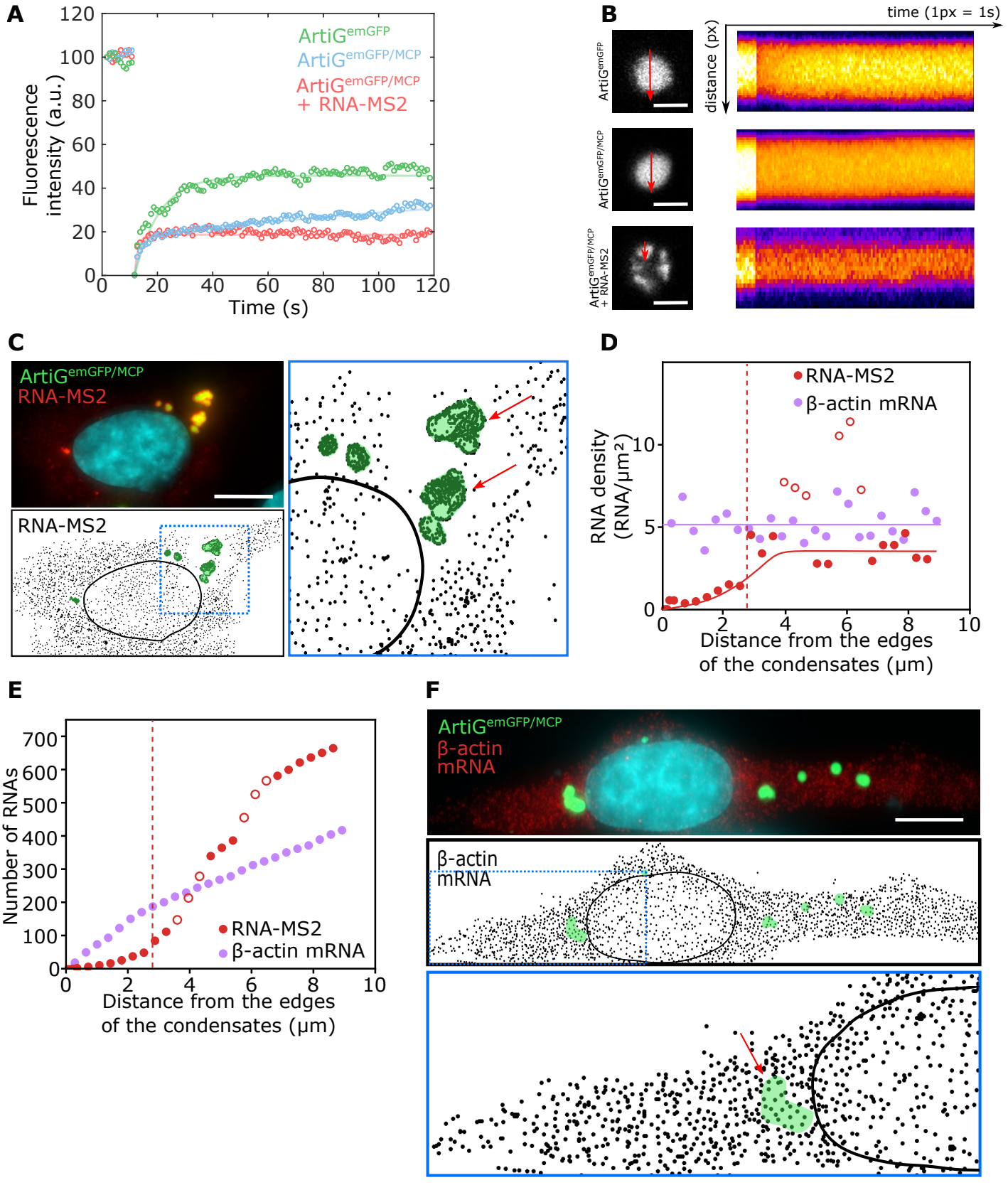

Figure 2: Fluorescence recovery after photobleaching and depletion of RNA-MS2 at the vicinity of ArtiG$^{emGFP/MCP}$ condensates. **A.** Fluorescence recovery after photobleaching performed on ArtiG^{emGFP} (green, 6 cells), ArtiG$^{emGFP/MCP}$ (blue, 8 cells) and ArtiG$^{emGFP/MCP/RNA}$ (red, 8 cells). Scale bar = 2 µm. **B.** Kymographs representation of three representative ArtiGs analyzed in **A**. **C.** Upper panel: epifluorescence imaging of ArtiG$^{emGFP/MCP}$ (green) and RNA-MS2 (red) in a Hela cell displaying a depletion of RNA-MS2 around the condensates. Scale bar = 10 µm. Lower panel: Binary mask of the RNA-MS2 molecules whose cooordinates have been acquired as described in the methods. Isolated dots are single RNA molecules while clustered dots overlap with ArtiG$^{emGFP/MCP}$ condensates (highlighted in green). The black solid line delineates the nucleus. The blue square is enlarged in the right panel. The red arrows point to the ArtiGs analyzed in **D** and **E**. **D.** Density of RNA-MS2 (red) and β-actin mRNA (violet) as a function of the distance from the ArtiG$^{emGFP/MCP}$ condensates indicated by red arrows in **C** and **F.** β-actin mRNA density is constant, while RNA-MS2 density reaches a plateau after the depletion area indicated by the red dashed line. Empty red dots correspond to RNA densities when crossing neighbouring condensates. **E.** Cumulative representation of the data shown in **D**. **F.** Upper panel: epifluorescence imaging of ArtiG$^{emGFP/MCP}$ (green) and β-actin mRNAs (red). Scale bar = 10 µm. Middle and lower panels: Binary mask of the β-actin mRNAs, as in **C**.

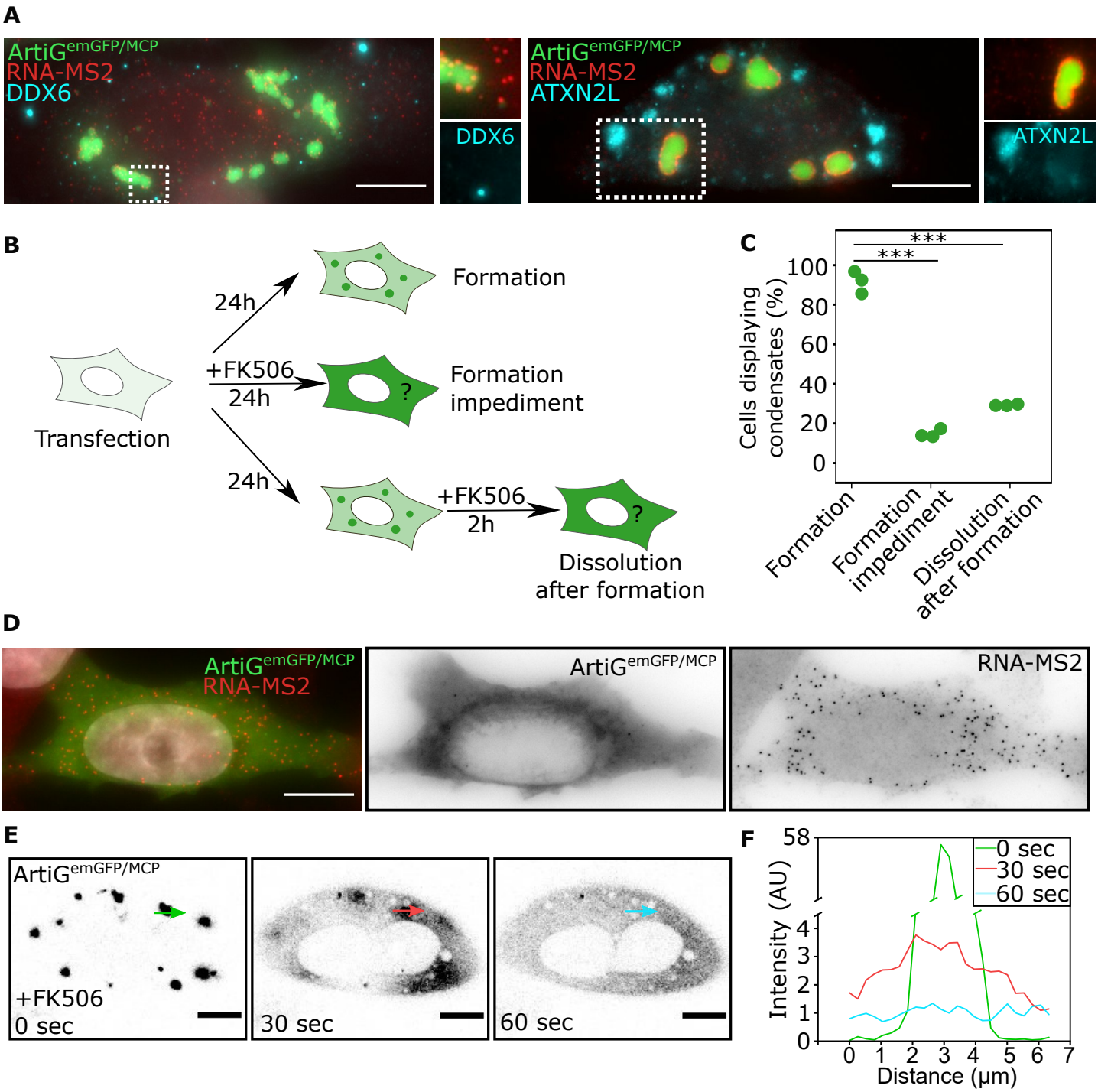

Figure 3: Absence of interaction of ArtiG$^{emGFP/MCP}$ with endogenous RNP granules, inhibition and reversibility. **A.** Epifluorescence imaging of ArtiG$^{emGFP/MCP}$ (green) and RNA-MS2 (red) in HeLa cells, after immunostaining of DDX6 (blue) as a PB marker (left panel) or ATXN2L (blue) as a SG marker (right panel). In the right panel, SGs were induced with arsenite for 30 minutes. White dashed rectangles delineate the images zoomed on the right. Scale bar = 10 µm. **B.** Experimental design to test the inhibition and reversibility of ArtiG$^{emGFP/MCP}$ formed in the presence of RNA-MS2, using FK506 in HeLa cells. FK506 was either added right after transfection to prevent condensation, or 24 h after transfection to dissolve the condensates. **C.** Percentage of transfected cells displaying ArtiG$^{emGFP/MCP}$ condensates in the absence of FK506 (Formation), when adding FK506 at the time of transfection (Formation impediment) or 24 h later for 2 h (Dissolution after formation). Differences between conditions with and without FK506 were statistically significant (p-values < 10^{-4} using a Student's t-test). **D.** Epifluorescence imaging of ArtiG$^{emGFP/MCP}$ (green) and RNA-MS2 (red) after condensate dissolution with FK506. Nuclei were stained with DAPI (blue). Scale bar = 10 µm. **E.** Confocal live imaging of ArtiG$^{emGFP/MCP}$ dissolution. FK506 was added at time zero. Colored arrows indicate where the intensity profiles in **F** were plotted. Scale bar = 10 µm. **F.** emGFP intensity profile across an ArtiG$^{emGFP/MCP}$ condensate over time (colored arrows in **E**).

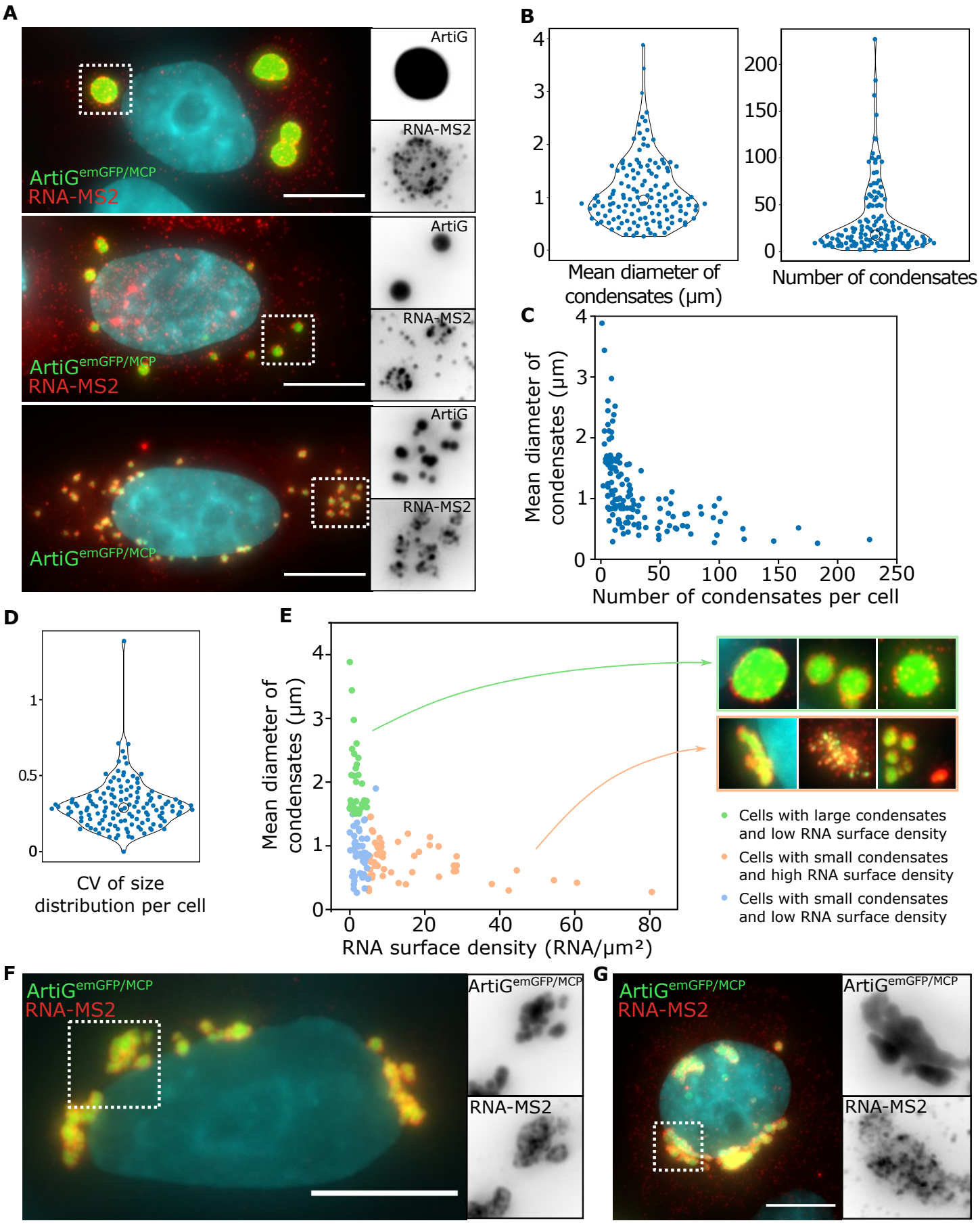

Figure 4: Heterogeneous morphology of ArtiG$^{emGFP/MCP}$ condensates. **A.** Epifluorescence imaging of three HeLa cells displaying different sizes and numbers of ArtiG$^{emGFP/MCP}$ in the presence of RNA-MS2. Cells were fixed 24 h after transfection of scaffold and RNA-MS2 plasmids (low RNA condition in the methods, i.e. 50 ng RNA-MS2). Scale bar = 10 µm. **B.** Distribution of the mean diameter of condensates per cell (left panel) and the number of condensates per cell (right panel), with each dot representing one cell (N = 140 from two independent experiments). **C.** Mean diameter of the condensates as a function of the number of condensates. **D.** Distribution of the coefficients of variation (CV) of the size distribution. **E.** Mean diameter of the condensates as a function of RNA surface density. Green and orange dots highlight cells displaying a mean diameter above or below 1.5 µm, respectively, and an RNA surface density below or above 5 molecules/µm², respectively. Images on the right show representative examples of condensates for the green and orange cell categories. **F. G.** Example of well-defined (**F**) and intertwining (**G**) condensate clusters.

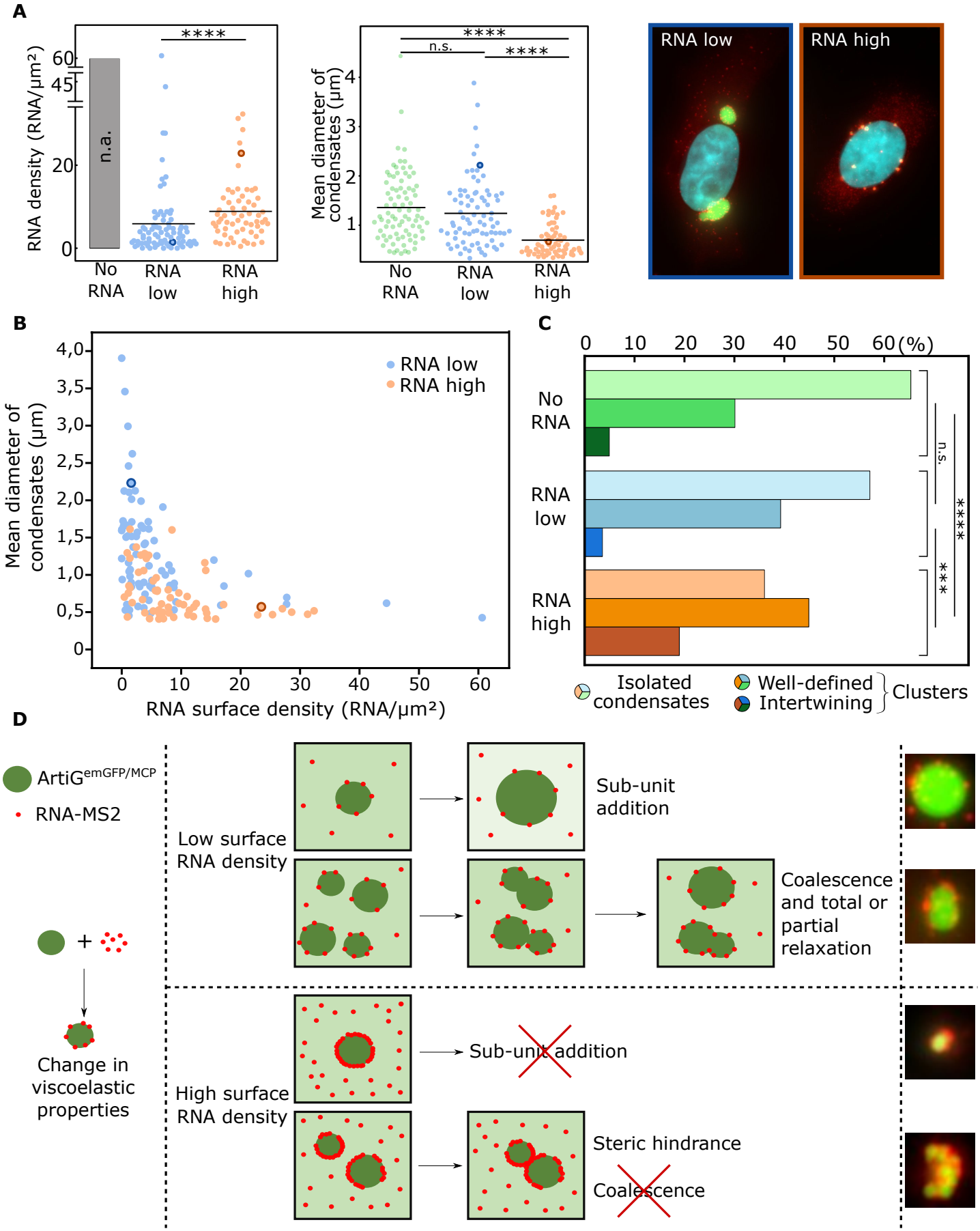

Figure 5: Impact of RNA density at the surface of condensates on condensate morphology. **A.** Distribution of RNA-MS2 density at the surface of condensates (left panel) and of mean diameter of the condensates (middle panel) in no RNA, RNA low and RNA high conditions, with each dot representing one cell (N = 82 for no RNA, N = 79 for RNA low and N = 64 for RNA high conditions, each from two independent experiments). Differences between RNA low and RNA high conditions were statistically significant using a Wilcoxon rank sum test (p-values < 10^{-5}). Representative epifluorescence images for RNA low and RNA high conditions are shown on the right and correspond to the circled dots in the graphs. **B.** Mean diameter of ArtiG$^{emGFP/MCP}$ in cells as a function of RNA-MS2 surface density in RNA low (blue dots) and RNA high (orange dots) conditions. **C.** Percentage of cells with ArtiG$^{emGFP/MCP}$ that display isolated condensates, clusters of well-defined condensates, or intertwining condensates, in no RNA, low RNA and high RNA conditions. Differences with and without RNA were statistically significant using a Pearson's chi-squared test (p-values < 10^{-6} and 10^{-4} for RNA low and RNA high, respectively). **D.** Schematic model of the impact of surface RNA molecules on condensate growth, material properties and coalescence. Illustrative examples of ArtiG$^{emGFP/MCP}$ (green) and RNA-MS2 (red) epifluorescence images are shown on the right.